The Banyan Tree Antenna Array

Steven S. Holland, *Student Member, IEEE*, and Marinos N. Vouvakis, *Member, IEEE*

***Abstract*—A new wideband, wide-scan array is introduced, called the Banyan Tree Antenna (BTA) array, that employs modular, low-profile, low-cost elements fed directly from standard unbalanced RF interfaces. The elements consist of vertically-integrated, flared metallic fins over a ground plane that are excited by a vertical two conductor unbalanced transmission line. The antenna resembles the bunny-ear or balanced antipodal Vivaldi antenna (BAVA) designs, but most importantly uses metallic shorting posts between the fins and the ground plane that suppress a mid-band catastrophic common-mode resonance that occurs in 2D arrays of balanced radiators fed with unbalanced feeds. This work introduces simple circuit models that describe key performance attributes of the BTA array, leading to unique physical insights and design guidelines. Simulations of infinite single- and dual-polarized BTA arrays have achieved approximately two octaves of bandwidth for VSWR < 2.2 at broadside and VSWR < 2.8 at scans out to $\theta = 45°$, while maintaining better than 14 dB polarization purity at $\theta = 45°$ in the D-plane.**

***Index Terms*—Antenna array feeds, antenna array mutual coupling, phased arrays, ultrawideband antennas, Vivaldi antennas.**

I. Introduction

WIDEBAND phased antenna arrays will be critical components of future multi-functional communication/sensing/countermeasure systems [1], which will utilize one or two wideband phased arrays to replace multiple antennas. Additional wideband array applications include wideband radar [2], radio telescopes [3], wideband communication systems [4], power combiners [5], and wideband reflector feeds [6]. These phased arrays have stringent electrical and manufacturing specifications that include wideband and wide-scan performance, multi-beam ability, and polarization agility.

Currently, arrays of tapered-slot end-fire radiators have been one of the most popular choices of wideband arrays in multi-functional systems [7]. The Vivaldi array [8], [9], has demonstrated bandwidths greater than 10:1 [10], [11], and wide-scan performance, while providing a direct connection to standard RF interfaces. When designed carefully, these arrays do not support common-modes, avoiding catastrophic resonances. Despite their desirable impedance performance, the Vivaldi array elements are long—namely, a length of $2.5\lambda_{\rm high}$ (where $\lambda_{\rm high}$ is the wavelength at the highest frequency) is needed for a 10:1 bandwidth and $\lambda_{\rm high}/2$ yields only a 2:1 bandwidth. This high profile leads to high cross-polarization levels when scanned in the D-plane. In addition, their elements are vertically-integrated and require electrical connection between them, making modular designs difficult. Nevertheless, some variations can be manufactured modularly, such as the body-of-revolution (BOR) [12] and Mecha-Notch [13] Vivaldi arrays, albeit with complicated fabrication.

The outstanding impedance performance of Vivaldi arrays has inspired the development of alternative low-profile tapered-slot configurations such as the Antipodal Vivaldi Antenna (AVA) [14], and the Balanced Antipodal Vivaldi Antenna (BAVA) [15], [16]. These elements are modular, thus easier to manufacture, and are only $\lambda_{\rm high}/2$ deep, leading to better D-plane cross-pol levels. However, two-dimensional (2D) arrays of these elemants can support a broadside common-mode that splits the operating band into two disconnected bands with approximately an octave of bandwidth. Balanced excitation through external baluns was identified as the key to eliminating the broadside common-mode resonance in 2D arrays. Differential feeding forces the push-pull mode currents to exist on the radiating fins, removing any common-mode components of the current altogether. One example of such an array is the bunny ear element [17], which is modular, low-profile, and has achieved bandwidths up to 5:1 [18]. The Doubly-Mirrored BAVA (DmBAVA) [19] incorporates mirroring that rotates elements 180° in the E- and H-planes of the array and uses a wideband hybrid to properly phase adjacent elements, achieving up to 5:1 bandwidths.

Although balanced excitation eliminates the broadside common-mode, these elements support common-modes when scanned in the E-plane [20] and [21]. Several methods of suppressing these scan-induced common-modes have been proposed in the literature. One method places metallic walls along the H-plane, effectively shielding adjacent elements, [22], [23], at the cost of increased fabrication complexity. Another approach is to place chip resistors between the fins and the ground plane near the end of the fins [17], or at the base of the element feed, as in [21], to dissipate the common-mode currents. This resistive loading lowers efficiency and power handling, and increases the noise temperature and fabrication/maintenance difficulty.

From the above discussion it is apparent that none of the current ultrawideband tapered-slot antenna array technologies are simultaneously modular and low-profile with low cross-pol while maintaining a direct connecttion to standard unbalanced RF interfaces. In an attempt to develop such a design, this paper introduces the Banyan Tree Antenna (BTA) array, which modularly achieves wideband/wide-scan performance without the need of external baluns, resistive loading, or metal H-plane walls. This is achieved with the addition of a novel shorting post arrangement at the tapered fins that is used to control the broadside common-mode resonance frequency. One can

Manuscript received April 24, 2010; revised October 20, 2010; accepted April 14, 2011. Date of publication August 12, 2011; date of current version November 02, 2011. This work was supported by the Naval Research Laboratory through Grant PG#11320000000008.

The authors are with the Department of Electrical and Computer Engineering, University of Massachusetts Amherst, Amherst, MA 01003 USA (e-mail: sholland@ecs.umass.edu).

Color versions of one or more of the figures in this paper are available online at http://ieeexplore.ieee.org.

Digital Object Identifier 10.1109/TAP.2011.2164177

view this modification as an integrated balun, thus alleviating the need for external baluns/hyrbids, allowing a direct connection to standard RF interfaces. Additionally, co-design of the integrated balun and antenna leads to better combined performance than that of an independently designed external balun and antenna. Thanks to the simple and insightful theory developed herein, BTA arrays can be designed to operate free of both the broadside common-mode and the scan-induced common-modes over 4:1 bandwidths in both single- and dual-polarized configurations with good matching out to $\theta = 45^\circ$ in all planes. Due to the low profile $(\lambda_{\rm high}/2)$ of the elements, the cross-pol levels are below -20 dB in the principle planes and better than -14 dB in the diagonal plane for dual-polarized designs.

The remainder of this paper is organized as follows. Section II discusses the broadside common-mode of 2D arrays of balanced elements fed with unbalanced feeds, and presents a simple model to predict its resonant frequency. Section III presents the topology of the Banyan Tree Antenna. Section IV develops the theory of operation of the Banyan Tree Antenna, using simple circuit models to provide physical insights and design guidelines. Section V presents results for a single- and a dual-polarized BTA. The paper concludes in Section VI.

II. Common-Mode Resonance

This section addresses the common-mode problem encountered in balanced arrays fed directly by unbalanced feeds.

1) Single-Polarized Arrays: Consider a single-polarized, doubly-periodic infinite array of balanced fins over a ground plane fed by unbalanced feed lines, as shown in Fig. 1, that is excited at broadside. This unbalanced feeding will induce differential, but unequal, currents on the two vertical fins, as shown by the arrows in Fig. 1. As a result, the currents on the vertical feed lines no longer cancel and a net flow of upward (in this case) current results on one conductor. This unequal current distribution between neighboring elements can excite a $\hat{\mathbf{z}}$-directed electric field much like the probe feeding arrangement of a cavity or a waveguide, shown in Fig. 9(a). When the distance between two vertical grounded conductors of neighboring elements in the array is equal to one half-wavelength, a field mode with dominant $\hat{\mathbf{z}}$-directed electric fields can be excited. This mode's fields do not radiate (reactive fields) and in turn induce $\hat{\mathbf{z}}$-directed (common-mode) electric currents on the metallic fins. Because the array is doubly periodic, a half-wavelength length between neighboring elements can be along the E-, H- or D-planes, as shown in Fig. 2. Any other resonant length between grounded conductors of non-neighboring elements is precluded due to the periodic nature of the array. Along the H-plane (L_H), no resonant mode can be excited because in this direction there is no probe-like feed conductor between grounded conductors. Along the E-plane (L_E), a resonant mode could be excited, but the un-equal currents at this frequency contribute to dominant radiated fields similar to those encountered in most dipole arrays. Both resonant lengths above correspond to frequencies close to the grating lobe frequency, and for scanning arrays they occur out-of-band. The resonant mode along the D-plane (L_D), is responsible for the dominant, problematic common mode, because the

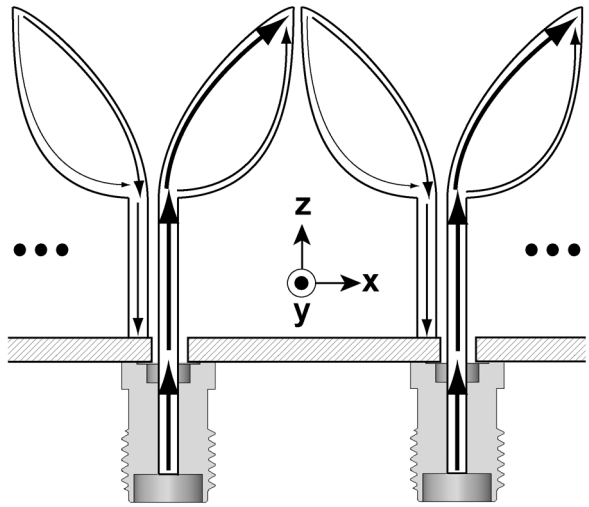

Fig. 1. Uneven differential-mode (push-pull) current densities due to the unbalanced excitation of balanced tapered-slot elements.

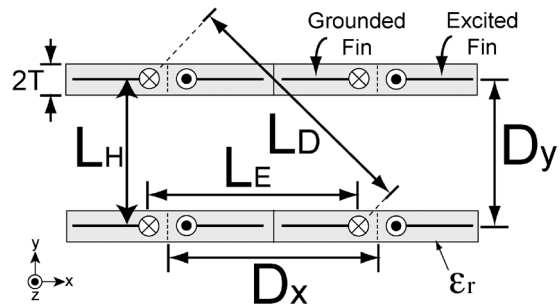

Fig. 2. Top view sketch of the array of Fig. 1. This model will be the basis for theoretically predicting the frequency of the common mode.

probe current has a component along this direction, as shown in Fig. 3, and the components of the horizontal radiated fields along this direction are small. Using $L_D = \sqrt{D_x^2 + D_y^2}$ as the resonant length, where D_x and D_y are the E- and H-plane spacings, respectively, the following common-mode resonance frequency is obtained:

$$f_{\rm cm} \approx \frac{c_{\rm o}}{2\sqrt{\epsilon_{r,\rm eff}}\sqrt{D_x^2 + D_y^2}} \tag{1}$$

where $c_{\rm o}$ is the speed of light in a vacuum, and $\epsilon_{r,\rm eff}$ is the effective relative permittivity given by

$$\epsilon_{r,\rm eff} = 1 + \frac{2T}{D_y}(\epsilon_r - 1) \tag{2}$$

where $2T$ is the thickness of the dielectric used to support the metallic fins (Fig. 2). The resulting common-mode currents on the fin conductors and the E_z field distribution near the ground plane are plotted at $f_{\rm cm}$ in Fig. 4.

To validate (1), the common mode frequency of a single-polarized array of elements shown in Fig. 8 (without shorting posts) with the parameters of Table I is considered. The array is analyzed using Ansoft/Ansys HFSS [24] and is compared to the theoretically calculated $f_{\rm cm}$ from (1), shown in Table II. The results show very good agreement, having less than 2% error for

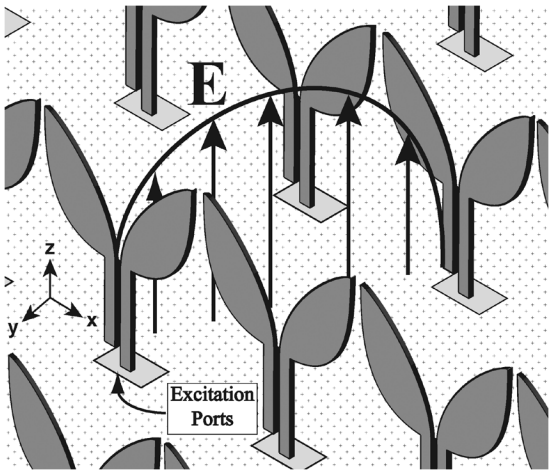

Fig. 3. Sketch of the resonant electric fields developed in the array of Fig. 1 at the common mode frequency (only the fields along the resonant length are shown).

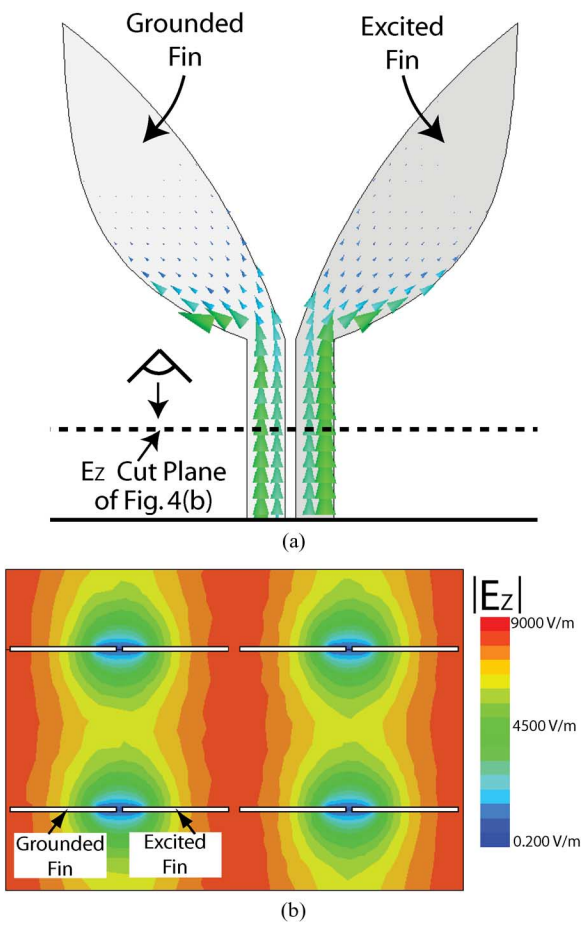

Fig. 4. Fields and currents in the unit cell of single-polarized, unbalanced fed fins scanned to broadside. (a) Electric currents on the element fins. (b) Overhead view of the $\hat{\mathbf{z}}$-polarized electric field magnitude, $|E_z|$ along the plane cut in Fig. 4(a).

various element spacings D_x and D_y, dielectric constants ϵ_r, and dielectric thicknesses $2T$, validating the proposed theory.

These insights can provide design guidelines for moving this resonance frequency out of band. One solution is to decrease

TABLE I
PARAMETERS USED FOR THE COMMON-MODE STUDIES

H [mm]	S [mm]	W_f [mm]	W_g [mm]
21.25	8.00	1.60	1.60
G [mm]	R_i [mm^{-1}]	R_o [mm^{-1}]	τ [mm]
0.45	0.10	-0.33	0.00

TABLE II
THEORETICAL VERSUS NUMERICAL f_{cm} IN SINGLE-POL ARRAYS

D_x [mm]	D_y [mm]	$2T$ [mm]	ϵ_r	$\epsilon_{r,eff}$	Theoretical f_{cm} [GHz]	Numerical f_{cm} [GHz]	Error
20	20	—	1	1	5.30	5.28	0.44%
20	15	2.0	2.2	1.16	5.57	5.53	0.73%
20	25	2.0	2.2	1.10	4.48	4.50	0.55%
20	20	2.0	2.2	1.12	5.01	4.95	1.22%
25	20	2.0	2.2	1.12	4.43	4.44	0.29%
20	15	6.0	5	2.60	3.72	3.67	1.37%
20	25	6.0	5	1.96	3.35	3.34	0.20%
20	15	4.0	10	3.40	3.25	3.20	1.66%
20	25	4.0	10	2.44	3.00	2.98	0.65%

f_{cm} and move it out of band by increasing either the E- or H-plane spacing of the elements (or both), but since the element spacings are constrained by grating lobe onset at D_x and $D_y = \lambda/2$, this option is deemed impractical. Another option is to move the common mode resonance up in frequency, by decreasing the element spacing. However, minimum spacing is limited by element size, and small element spacing results in a large T/R module count. Unlike the element spacing, which has an inverse relationship to f_{cm}, the dielectric constant $\epsilon_{r,\mathrm{eff}}$ has an inverse square root relationship to f_{cm}, resulting in only a modest shift in resonant frequency for a $\Delta\epsilon_{r,\mathrm{eff}}$. It is clear that these parameters alone cannot successfully move the resonance out of the operating band. The BTA modifies the element topology to introduce additional design degrees of freedom that are used to shift the common mode out of band, as will be elaborated in Sections III and IV.

This common-mode resonance is excited strongly at broadside where the fields of the array are in phase at each element. Scanning off broadside in any plane introduces a phase progression in the fields that, since that the fields are no longer in phase at neighboring elements, reduces the strength of the resonance excitation. Fig. 5 shows the impedance for scanning along the E-plane near f_{cm} of a single-polarized array with parameters in Table I. At broadside, the impedance swings through a series resonance with $R = 0\ \Omega$. As θ increases, the resonance is excited weakly and the loci quickly contract toward the center of the Smith chart. When the elements are embedded in a dielectric, the strength of the common mode excitation falls off slower with θ, and f_{cm} increases with θ as a function of $\cos\theta$ (substituting D_x with the effective length, $D_x \cos\theta$, in (1), where the E-plane is assumed to be the xz-plane). The common-mode resonance disappears along D- or H-plane scanning, for both dielectric and dielectric-free arrays. As a result, moving f_{cm} above the operating band at broadside implies common-mode free scanning operation.

It is important to note that the common-mode described in this section is unique to unbalanced fed arrays only. Balanced fed elements do not support this particular mode, but instead suffer

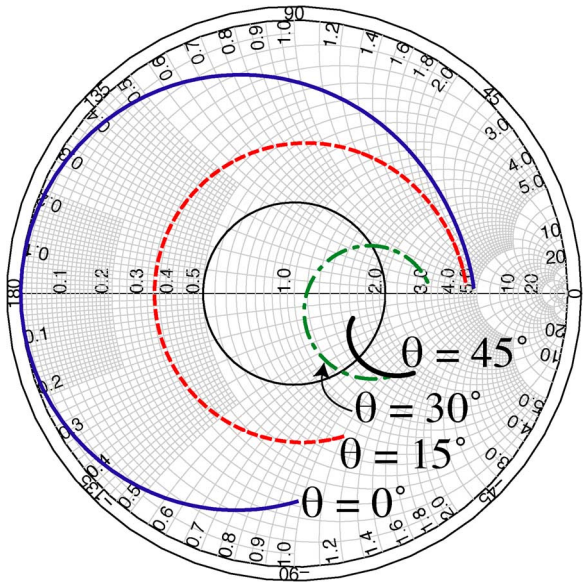

Fig. 5. Impedance variation of the arrays in Figs. 1 and 3 near $f_{\rm cm}$ for various scanning angles in the E-plane.

from other common-modes that, while not excited at broadside, appear with E-plane scan [20], [21], [23], [25].

2) Dual-Polarized Arrays: In dual-polarized arrays the topology is altered by the presence of the orthogonal set of fins. A top view of a dual-polarized unit cell and some important dimensions are shown in Fig. 6. Because the orthogonal fins provide vertical grounded conductors that lie exactly in the middle of L_D, the common mode described in the previous subsection is shifted to twice the frequency, well above the operating band. In this case, the resonant length responsible for the problematic common mode is that of L_E, for the reasons described in the previous subsection. Thus, in dual-pol arrays $f_{\rm cm}$ can be predicted by

$$f_{\rm cm} \approx \frac{c_\circ}{2\sqrt{\epsilon_{r,\rm eff}}D} \tag{3}$$

where $D = \min\{D_x, D_y\}$. Again, the effective relative permittivity, $\epsilon_{r,\rm eff}$, is found using the same weighted average method, and results in

$$\epsilon_{r,\rm eff} = 1 + \left(\frac{2T[D_x + D_y] - 4T^2}{D_x D_y}\right)(\epsilon_r - 1). \tag{4}$$

The common mode now occurs at the grating lobe frequency f_g for dielectric-free arrays, and inside the operating band of arrays with dielectric. Most practical dual-polarized arrays of balanced radiators with unbalanced feeding use dielectrics to support the conductors and do have a common-mode inside the operating band. Table III shows good agreement between numerical and theoretical calculations of $f_{\rm cm}$, with less than 2% error.

III. Banyan Tree Antenna (BTA) Array

The common-mode was shown to limit the performance of balanced elements fed with an unbalanced feed, and in response the Banyan Tree Antenna (BTA) array has been developed to alleviate this problem.

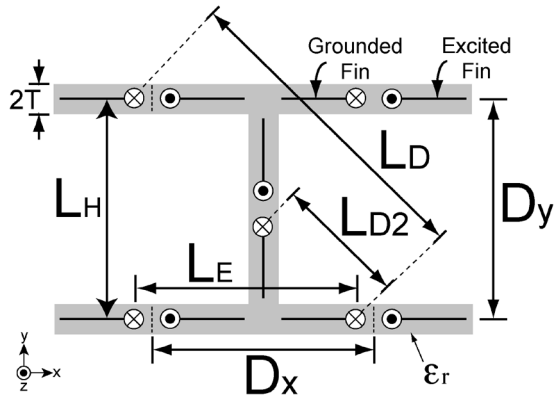

Fig. 6. Top view sketch of the the dual-polarized array of Fig. 1.

TABLE III
Theoretical Versus Numerical $f_{\rm cm}$ in Dual-Pol Arrays

$D_x = D_y$ [mm]	$2T$ [mm]	ϵ_r	ϵ_{reff}	Theoretical f_{cm} [GHz]	Numerical f_{cm} [GHz]	Error
20	2.0	2.2	1.23	6.77	6.91	2.05%
26	2.0	2.2	1.18	5.32	5.22	1.85%
32	2.0	2.2	1.15	4.38	4.36	0.46%

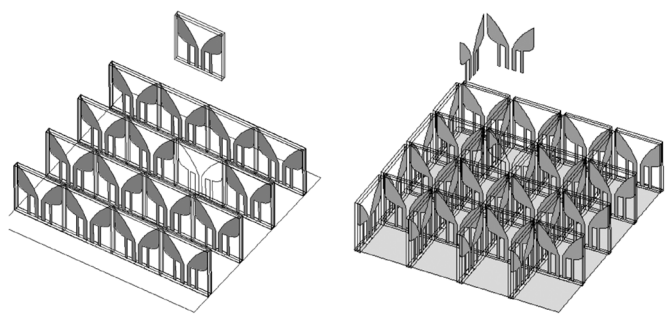

Fig. 7. BTA array arrangements: (a) single-polarized, and (b) dual-polarized (egg-crate grid).

Single- and dual-polarized arrangements of the BTA elements on a rectangular, egg-crate lattice are shown in Fig. 7(a) and (b), respectively. Elements do not require electrical continuity and are arranged with gaps between neighbors, allowing for modular construction.

The topology, along with the main geometric design parameters of the BTA element, is shown in Fig. 8. Vertical shorting posts connect the radiating fins to the ground plane, and are the key to controlling the common-mode resonance frequency, which will be discussed in detail in Section III-A. These shorting posts resemble the vertical root system of the distinctive Banyan tree, hence the origin of the array's name. This paper focuses on printed BTAs, namely a single metal layer embedded between two equal thickness dielectric slabs, as shown in the side view in Fig. 8. Other variations on the fabrication method are possible and can be found in [26], [27]. An individual element consists of two exponentially tapered fins with inner and outer flare rates of R_i and R_o, respectively, oriented vertically over a ground plane. Together, the fins effectively form a tapered slot structure in the void between the fins. However, due to the extremely

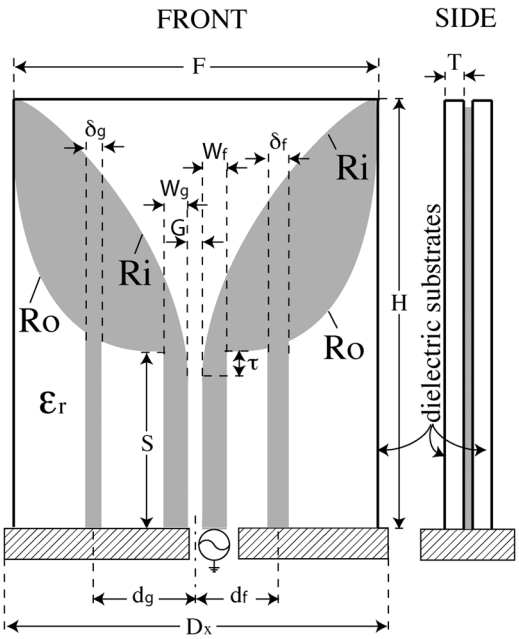

Fig. 8. Element topology and main geometrical design parameters of the Banyan Tree Antenna (BTA) element.

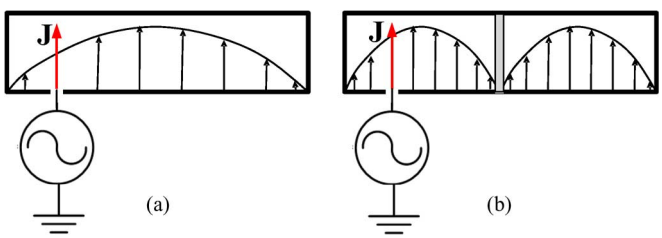

Fig. 9. Mode excitation and mode suppression principles. (a) Fundamental mode excitation with current source (see Fig. 3 for BTA analogy). (b) Control of fundamental mode through shorting via.

short length of this tapered slot (total element height typically $< \lambda_{\text{high}}/2$), the fins operate more like fat, capacitive dipoles with an exponentially flared matching section over a ground plane.

At the aperture of the array, the impedance is typically ≈150–200 Ω. Matching this large impedance to 50 Ω poses a formidable challenge, especially over a wide bandwidth. The exponentially tapered fins and the short vertical feeds act as an integrated impedance matching circuit that allows the input impedance at the ground plane to be well matched to 50 Ω.

The vertical feed consists of a pair of printed strips that form an unbalanced feed line of length S, where one line is connected to the ground plane, and the other is fed directly from an unbalanced T-line, i.e., a standard RF interface. Thus, the BTA connects directly to unbalanced feed network T-lines or T/R modules below the ground plane, without the need of an external balun or hybrid.

The use of unbalanced feed lines is possible because of the additional printed lines, referred to as shorting posts, which directly short the fins to the ground plane. Prudent placement of the shorting posts forces electric field nulls that modify the common-mode resonant length L_D, providing a means of controlling the common mode resonance frequency. This will be thoroughly explained in Section IV-A.

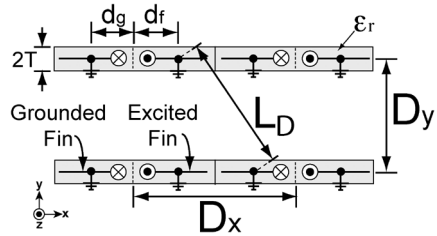

Fig. 10. Model used to theoretically predict the common mode frequency in a BTA array.

IV. Theory of Operation

The BTA has a complex geometry that requires rigorous full-wave numerical analysis for evaluation and optimization of the array. Nevertheless, a simple approximate theory will be developed to predict the occurrence of important performance-limiting resonances as well as to provide physical insight into controlling the BTA operation.

A. Common-Mode Control With Shorting Posts

1) Single-Polarized Arrays: As shown in Section II, modifications of the geometry or materials in the traditional structure of Fig. 1 are unable to shift the common-mode frequency out of band. A solution emerges when one considers modifying the topology in order to introduce additional degrees-of-freedom into the length L_D expression. This is done in the BTA by inserting shorting posts between the fins and the ground plane, strategically forcing the electric field to zero. Much like the PCB mode suppression vias used to shift troublesome cavity resonances [Fig. 9(b)] out of the desired range, the shorting posts of the BTA constrain the resonant fields to smaller resonant lengths, shifting the resonant frequency upwards.

A top view of the BTA unit cell is shown in Fig. 10, showing the location of the BTA shorting posts. It is clear that the diagonal length L_D is now shorter, and the common-mode resonant frequency is approximately

$$f_{\text{cm}} \approx \frac{c_\circ}{2\sqrt{\epsilon_{r,\text{eff}}}\sqrt{(D_x - d_f - d_g)^2 + D_y^2}} \tag{5}$$

where d_f and d_g are the distances between the center of the element and the shorting post on the fed and grounded fins, respectively, as shown in Fig. 8. For comparison, an exemplary BTA design with design parameters shown in Table I and with the addition of shorting posts of width $\delta_g = \delta_f = 0.3$ mm is considered for various shorting post locations $d = d_g = d_f$, and with $D_x = D_y = 20$ mm. The fins are printed on Rogers 5880 ($\epsilon_r = 2.2$) of thickness $T = 1.0$ mm. The broadside VSWR for these cases is shown in Fig. 11. As the shorting post spacing is increased, the frequency of the large spike in the VSWR due to the common-mode resonance increases; in this case, the common-mode is shifted from 4.9 GHz to nearly 7 GHz. The numerical results are compared to the theoretical predictions from (5) in Table IV. The analytic results are within 4% of the numerical results, showing excellent agreement.

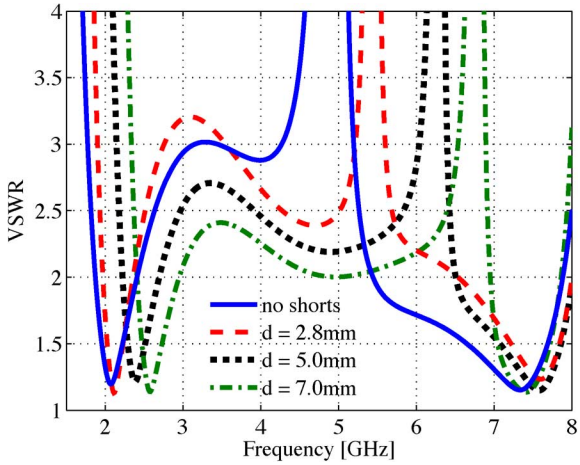

Fig. 11. Variation of the common-mode resonance as a function of the shorting post position for a single-pol BTA array.

TABLE IV
THEORETICAL VERSUS NUMERICAL PREDICTION OF $f_{\rm cm}$ IN SINGLE-POL BTA

$d_f = d_g$ [mm]	Theoretical f_{cm} [GHz]	Numerical f_{cm} [GHz]	Error
(no shorts)	5.01	4.95	1.22 %
2.8	5.75	5.54	3.67 %
4.0	6.08	5.99	1.50 %
5.0	6.34	6.28	0.96 %
6.0	6.58	6.62	0.60 %
7.0	6.78	6.76	0.30 %

TABLE V
THEORETICAL VERSUS NUMERICAL PREDICTION OF $f_{\rm cm}$ IN DUAL-POL BTA ARRAYS

$D_x = D_y$ [mm]	$d_f = d_g$ [mm]	$2T$ [mm]	ϵ_r	ϵ_{reff}	Theoretrical f_{cm} [GHz]	Numerical f_{cm} [GHz]	Error
30	2.8	2.0	2.2	1.15	5.13	4.95	3.66%
30	4.0	2.0	2.2	1.15	5.36	5.41	0.77%
30	6.0	2.0	2.2	1.15	5.81	6.02	3.40%

2) Dual-Polarized Arrays: In dual-polarized arrays, (3) is modified to account for the shorting posts, and results in

$$f_{\rm cm} \approx \frac{c_\circ}{2\sqrt{\epsilon_{r,\rm eff}}(D - d_g - d_f)} \tag{6}$$

where $D = \max\{D_x, D_y\}$. Table V shows good agreement between numerical and theoretical calculations from (6) of $f_{\rm cm}$ in a dual-pol BTA array, using the element of Section IV-A1. In dual-polarized BTA arrays, the common-mode is readily moved out of the operating band, above f_g, since the common-mode is already near the high end of the operating band. In fact, the shorting posts move $f_{\rm cm}$ well above f_g, which can further increase the bandwidth for applications requiring only a limited scan volume.

While the shorting posts are effective in controlling the common-mode resonance, their presence affects the operation over the rest of the band, as shown in Fig. 11. The remaining sections discuss the theory of operation over these bands and highlight design implications and compromises.

TABLE VI
COMPARISON OF LOOP-MODE RESONANCE THEORY WITH NUMERICAL SIMULATION

D_x [mm]	S [mm]	Theoretical f_{loop} [GHz]	Numerical f_{loop} [GHz]	Error
15.0	8.00	1.71	1.65	3.64 %
20.0	8.00	1.60	1.53	4.58 %
25.0	8.00	1.51	1.42	6.33 %
20.0	4.00	2.01	2.12	5.18 %
20.0	6.00	1.73	1.84	5.98 %
20.0	12.00	1.18	1.23	4.07 %
20.0	16.00	1.03	0.99	4.04 %

B. Transmission Line Model of Shorting Posts

Having explored the effect of the shorting posts on the common-mode resonance frequency, their impact on the array impedance over the remainder of the band is now considered using elementary transmission line models.

Modeling the impedance seen at the beginning of the fins (and absent of shorts) as $Z_{\rm ant}$, four distinct transmission lines can be identified due to the two feed lines and the two shorting posts. The first transmission line is formed by the vertical feeds, as in Fig. 12(a). The remainder of the transmission lines can be identified as shown in Fig. 12(b)–(d). A full transmission line model is shown in Fig. 12(e), where the lines Z_2, Z_3, Z_4 are shown in parallel with $Z_{\rm ant}$, which is fed via transmission line Z_1. The shorting post transmission lines are approximately a quarter-wavelength at mid-band, appearing as an open circuit at the location of $Z_{\rm ant}$, leaving the impedance unaffected. Therefore, despite providing a direct DC path between the fins and the ground plane, the shorting posts do not short out the radiating currents at mid-band and high frequencies. At low frequencies, the shorting post transmission lines are electrically short, and they look like short circuits in parallel with $Z_{\rm ant}$; this results in the excitation of a loop mode that is explored in the next section.

C. Low Frequency Loop-Mode Resonance

While the upper limit of the operating band is primarily dictated by the grating lobe frequency, the BTA has a low frequency limit defined by a sharp loop-mode resonance that has a large spike (ideally infinite in height) in the resistance and a large resonant swing of the reactance typical of a parallel resonance. This resonance is a consequence of the shorting posts, which at low frequencies provide a low impedance path for currents, thus allowing a current path to form a resonant loop between elements along the E-plane. The effects of this resonance can be seen in Fig. 11 as a shift of the low end band-edge. The resonant loop can be seen by examining the currents on the fins of the BTA at the loop-mode resonance frequency, as shown in Fig. 13(a). The generator excites currents on the vertical feed stem, which flow onto the fin section of the element. The current, instead of continuing to flow along the inner and outer edges of the fin, is shunted to the ground plane through the shorting post, and additional current flows from the top of the fin down into the shorting post. On the grounded fin, the currents are similar to those in regular operation, with currents on the shorting posts and feed lines flowing in the same direction. Considering image theory in Fig. 13(b), two distinct loop paths can be identified as

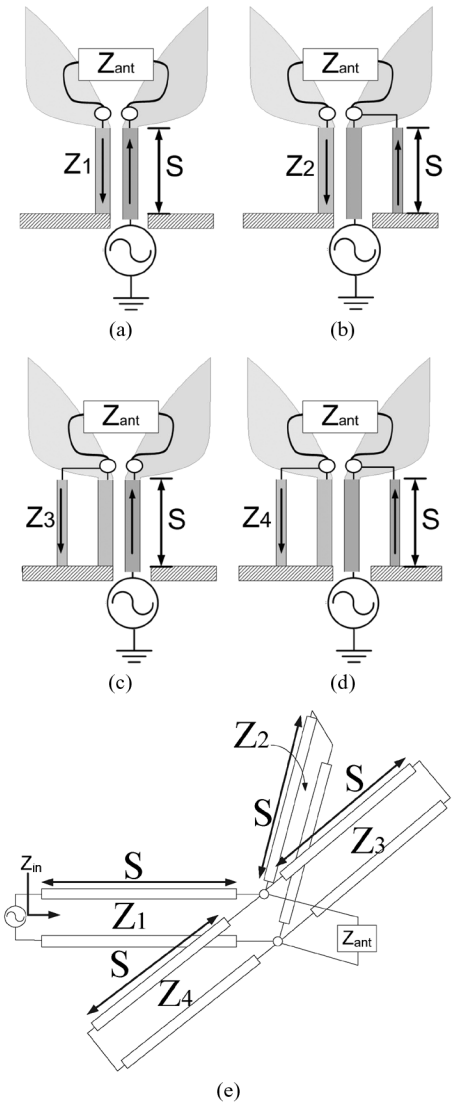

Fig. 12. Transmission line models of the BTA. (a) The feed lines are modeled with T-line impedance Z_1, and the shorting posts are modeled as three T-lines (b) Z_2, (c) Z_3, (d) Z_4 connected in parallel with the feed lines, as shown in (e).

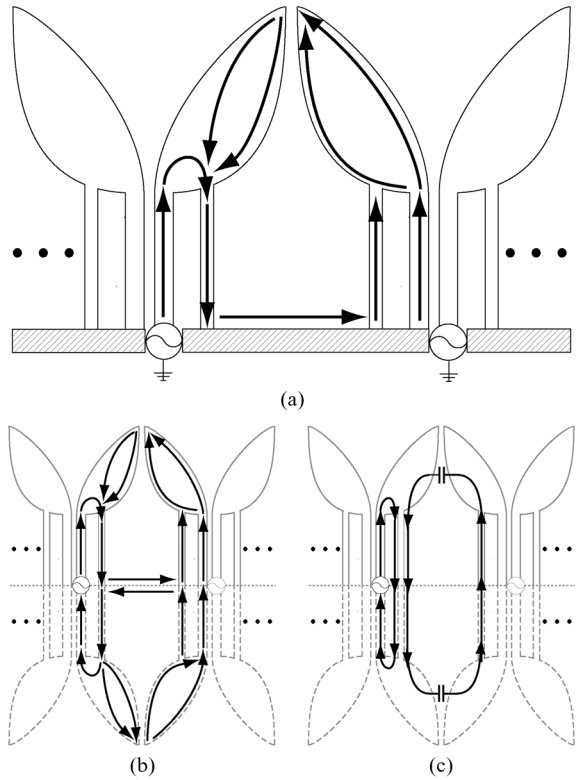

Fig. 13. The loop-mode resonance in the BTA. (a) Current distribution around the loop-mode resonance (low frequency of operating band). (b) Current distribution using image theory. (c) Effective resonant current loop paths on the fins.

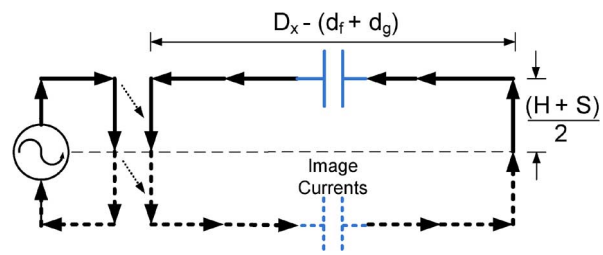

Fig. 14. Loop-mode circuit model consisting of a non-resonant driving loop (left) coupling energy into a large half-wave resonant loop.

in Fig. 13(c), where two loops are shown to share close proximity along one arm of each loop, producing high coupling. From a loop antenna perspective, these coupled loops can be modeled as shown in Fig. 14, where a small driver loop couples strongly to a large resonant loop. The capacitive coupling between neighboring elements is represented by a lumped capacitance inside the resonant loop. The length of the resonant loop was estimated using known lengths in the element geometry. By expressing the approximate length of the loop as $l_{\text{loop}} = 2(H + S + D_x - (d_g + d_f)) = \lambda_{\text{loop}}/2$, the approximate loop-mode resonant frequency is given by

$$f_{\text{loop}} \approx \frac{c_\circ}{4\sqrt{\epsilon_r}\,(H + S + D_x - (d_g + d_f))} - |f(C)| \qquad (7)$$

where $|f(C)|$ is a non-negative function of the capacitance used to account for the effects of capacitive coupling between neighboring fins. Table VI shows theoretical and numerical results (Ansoft/Ansys HFSS [24]) predicting f_{loop} for the design of Table I, with the addition of shorting posts of width $\delta_g = \delta_f = 0.3$ mm at locations $d_g = d_f = 6.2$ mm, printed on Rogers 5880 ($\epsilon_r = 2.2$) of thickness $T = 0.787$ mm, and with $|f(C)| = 0$; the results demonstrate good agreement with less than 7% error, even without using $|f(C)|$.

Since $(d_g + d_f) \ll H + S + D_x$, the loop-mode resonance frequency is not a strong function of the shorting post separation. However, the loop-mode resonant width (inversely proportional to the quality factor Q_{loop}) increases directly with d_f and d_g, such that a larger frequency range around f_{loop} is affected by the resonance. This is evident in Fig. 11, where the low frequency limit of the operating band increases as the common-mode is shifted upward in frequency. This indicates an inherent compromise between moving the common-mode out of band and maintaining operation at low frequencies. To help alleviate the low-frequency degradation, strategies for decreasing f_{loop} or increasing Q_{loop} are required.

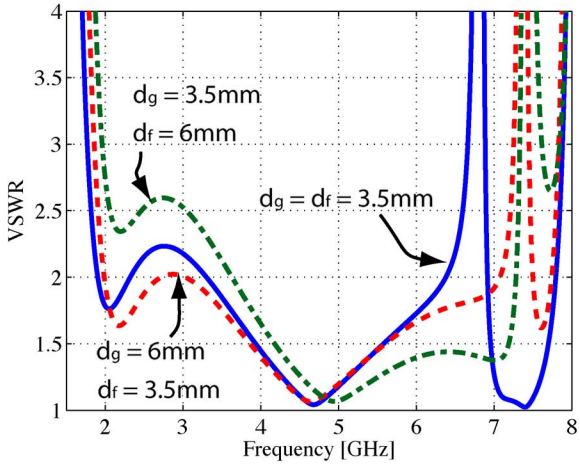

Fig. 15. Effect of shorting post asymmetry on the VSWR of the single-pol BTA.

Equation (7) indicates that there are three distinct ways of lowering the loop resonance frequency f_{loop}. The first is to increase the E-plane spacing D_x to add length to the loop, but this is a poor option since it lowers the grating lobe onset frequency. The second method is to increase the vertical feed line height S, which can significantly increase the length of the resonant loop. Finally, the third method is to increase the capacitive coupling between E-plane neighbors, which is primarily controlled through the separation of neighboring fins, and the area of the fins (e.g., large values of R_o). However, the minimum fin separation is limited by fabrication constraints. Also, high capacitive coupling results in large resonant impedance swings at the second order resonance of the loop mode, which constitutes itself as a VSWR hump around 3.2 GHz in Fig. 11. Among these methods, it was found that the width of the feed lines W_g and W_f and the height S of the fins over the ground plane, along with asymmetric shorting post placement, provide a good design compromise.

To demonstrate the effect of this asymmetric shorting post placement on the BTA, Fig. 15 shows three example cases, where the shorting posts are placed symmetrically with $d_f = d_g = 3.5$ mm, asymmetrically with $d_f = 3.5$ mm and $d_g = 6$ mm, and asymmetrically with $d_f = 6$ mm and $d_g = 3.5$ mm. In the latter two cases, f_{cm} occurs at the same frequency, since the overall separation between the two shorting posts is equal. However, when d_f is equal to 6 mm, the low frequency limit increases, and the match worsens over the low frequencies. When d_g is increased to 6 mm, the match improves at the low frequencies. For asymmetric placement of the shorting posts, (5) remains valid. More importantly, the cross-polarization studies in the next section indicate that the asymmetric short locations do not lead to increased cross-pol levels.

V. Design Examples

The theory developed in the previous section leads to unique physical insights that can be used (along with the tuning via full-wave analysis) to design a single- and dual-polarized BTA array operating over the band of 2–7.5 GHz. It is noted that no extensive bandwidth optimization was attempted and it is believed that the bandwidth enhancement techniques described in [19] can be readily applied in the BTA. All numerical results were obtained using infinite array analysis with Ansys/Ansoft HFSS 11 [24]. All results are referenced to a 50 Ω waveport impedance, and use real dielectric materials, but infinitely thin perfect electric conductors. A $1.6\lambda_{\text{high}}$ long air box terminated with a $\lambda_{\text{high}}/4$ thick PML is used for the simulations.

TABLE VII
Single-Pol BTA Array Dimensions

D_x [mm]	D_y [mm]	F [mm]	T [mm]
20.00	15.00	19.25	0.79 (31mil)
d_g [mm]	d_f [mm]	δ_g [mm]	δ_f [mm]
6.40	3.50	0.25	0.25
H [mm]	S [mm]	W_f [mm]	W_g [mm]
25.25	12.00	2.70	2.70
G [mm]	R_i [mm^{-1}]	R_o [mm^{-1}]	τ [mm]
0.10	0.10	-0.70	2.00

A. Single-Polarized BTA

A simple rectangular grid, similar to that depicted in Fig. 7(a), is utilized for the single-polarized BTA array. The array element is depicted in Fig. 8, where the E-plane element spacing is $D_x = 2$ cm, and the H-plane spacing $D_y = 1.5$ cm. This grid leads to a grating lobe onset frequency of $f_g = 7.5$ GHz (assuming scan at $\theta_\circ = 90°$) in the E-plane, and $f_g = 10$ GHz in the H-plane. The elements are printed on Rogers 5880 dielectric ($\epsilon_r = 2.2$), and a detailed description of the element dimensions can be found in Table VII.

The loop mode resonance described in Section IV-C has a Q_{loop} that decreases as d_g and d_f are increased, and thus d_f and d_g should be minimized when possible. In addition, the shorting posts are not symmetrically arranged on each fin of the element. Instead, the shorting post on the fed fin is located at $d_f = 3.5$ mm from the center, while the shorting post on the grounded fin is located at $d_g = 6.5$ mm.

1) Scan Impedance: The infinite array VSWR performance of the single-pol BTA array is shown in Fig. 16, at scans out to $\theta = 45°$ in the E- and H-planes (note that the vertical lines at 2 and 7.5 GHz indicate the edges of the operating band). The impedance is well behaved with scan, exhibiting the highest VSWR when scanned to $\theta = 45°$, VSWR <2.2, in the E-plane, while the maximum VSWR = 2.9 in the H-plane. The higher VSWR in the H-plane is typical for this type of element. Although not shown here, the D-plane VSWR results are an approximate average of the principal plane VSWRs.

2) Cross-Polarization: Infinite arrays radiate a discrete spectrum of plane waves (Floquet modes). The main lobe of radiation can be decomposed into two orthogonally polarized plane waves propagating in the scan direction. In order to obtain the radiated power carried by these polarizations, a surface S parallel to the ground plane is defined some distance from the array. Power flowing through this surface can be calculated by integrating the Poynting vector over the surface, using field components defined by Ludwig's third definition of co- and cross-polarization [28], providing the radiated power per unit cell area. The co- and cross-polarized radiated powers per unit cell are shown in Fig. 17 versus frequency for scanning in the E- and

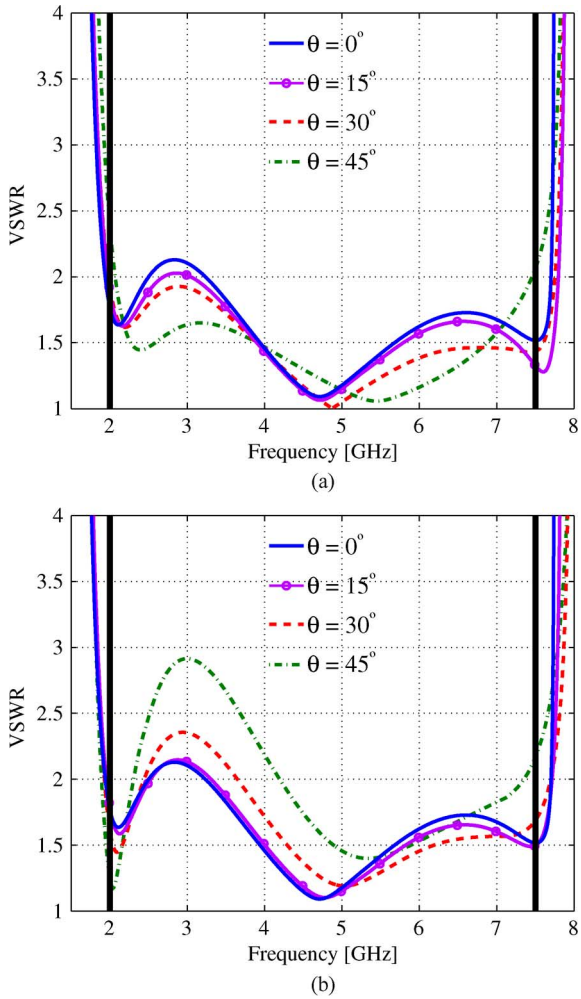

Fig. 16. VSWR versus frequency and scan angle of the infinite single-polarized BTA array. (a) E-plane; (b) H-plane. The D-plane impedance (not shown here) is approximately the average of the two.

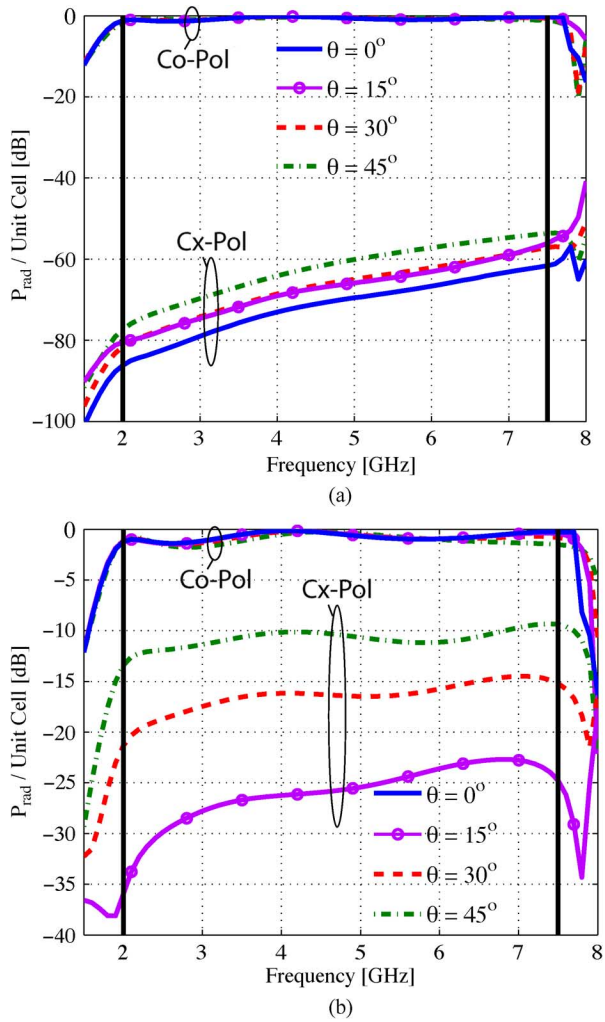

Fig. 17. Co- and cross-polarization radiated power versus frequency and scan angle of the infinite single-polarized BTA array. (a) E-plane; and (b) D-plane. The H-plane polarization levels (not shown here) are approximately the same as the E-plane.

D-planes, plotted in dB and normalized to the incident power at the input port; therefore, these levels include mismatch losses.

For all scan angles, the co-polarized power is nearly 0.1 dB down from the input power over the full frequency band, indicating high efficiency. The co-polarization level is shown to slightly decrease near 3 GHz, where the VSWR approaches 2 (an impedance match of VSWR $= 2$ has an insertion loss of 0.5 dB due to mismatch). When scanning along the E-plane, the cross-polarization is well below -50 dB, since this plane preserves symmetry and the currents on the vertical feed lines radiate the same polarization as the currents along the fins.

Scanning along the D-plane shows higher cross-polarization levels since the vertical components of the current on the feed lines and fins radiate power that is orthogonally polarized to the main beam, substantially adding to the cross-polarization level. The H-plane, although not shown for the sake of brevity, is below -20 dB for all angles.

B. Dual-Polarized BTA

Next, an egg-crate, rectangular grid dual-polarized BTA array is analyzed, as shown in Fig. 7(b). The design is based upon the single-polarized element in Section V-A with some modifications due to both mechanical and electrical considerations introduced by the dual-polarized arrangement. The element spacing is equal in both planes, chosen as $D_x = D_y = 2$ cm for a grating lobe frequency $f_g = 7.5$ GHz. The elements are printed on Rogers 5880 dielectric ($\epsilon_r = 2.2$), and a detailed description of all design parameters is shown in Table VIII. The shorting posts are now symmetrically placed on each of the element fins, with $d_f = d_g = 3.5$ mm. This is possible since the dual-polarized arrays have an f_{cm} that occurs at a higher frequency than in the single-polarized arrays.

1) Scan Impedance: Fig. 18 shows the infinite array VSWR performance, with the $\hat{\mathbf{x}}$-polarized elements excited and the $\hat{\mathbf{y}}$-polarized elements terminated in 50 Ω loads. The coupling between the two polarizations was found to be very low, better than -25 dB in the principle planes and -15 dB in the D-plane, but is not included due to space limitations. The D-plane VSWR is approximately an average of the principle plane VSWRs, thus are omitted for brevity. The E-plane VSWRs have a VSWR $<$ 2.0 over all scan angles, for the full band of 2–7.5 GHz (3.75:1

TABLE VIII
DUAL-POL BTA ARRAY DIMENSIONS

D_x [mm]	D_y [mm]	F [mm]	T [mm]
20.00	20.00	18.40	0.79 (31mil)
d_g [mm]	d_f [mm]	δ_g [mm]	δ_f [mm]
3.20	3.20	0.25	0.25
H [mm]	S [mm]	W_f [mm]	W_g [mm]
22.50	9.00	2.00	2.50
G [mm]	R_i $[mm^{-1}]$	R_o $[mm^{-1}]$	τ [mm]
0.10	0.10	-0.65	0.00

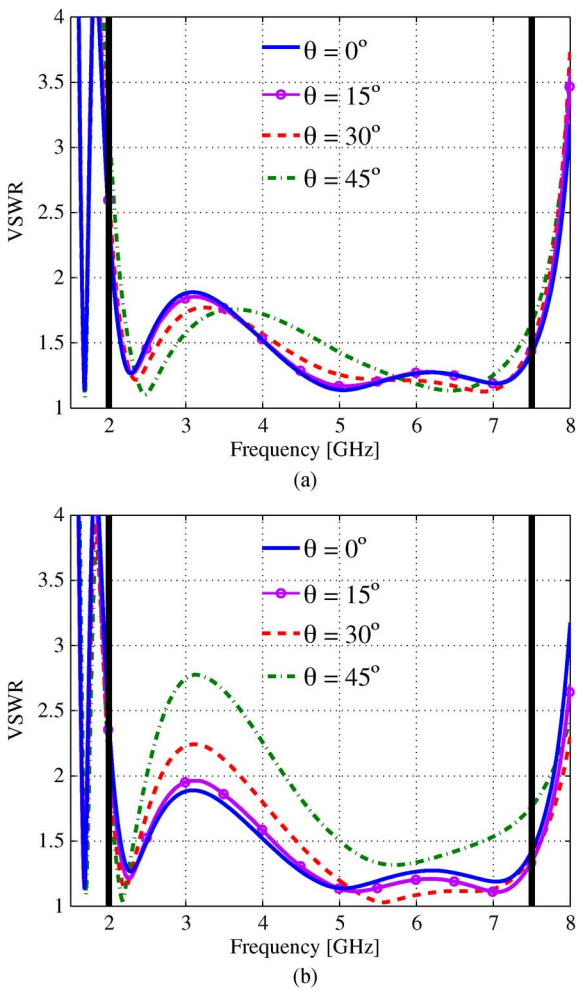

Fig. 18. VSWR versus frequency and scan angle of the infinite dual-polarized BTA array. (a) E-plane; (b) H-plane. The D-plane impedance (not shown here) is approximately the average of the two.

bandwidth). Along the H-plane, the VSWR again shows the characteristic increase with θ, reaching a maximum VSWR $=$ 2.8 at 3 GHz.

2) Cross-Polarization: The co- and cross-polarization levels for the dual-polarized BTA array are plotted in Fig. 19 for scanning along the E- and D-planes. The $\hat{\mathbf{x}}$-polarized elements are excited and the $\hat{\mathbf{y}}$-polarized elements are terminated in 50 Ω loads. As in the single-polarized BTA, the efficiency of the dual-polarized array is very high, decreasing slightly near 3 GHz due to the mismatch loss of 0.5 dB at VSWR $=$ 2. This high efficiency also indicates very low coupling of power between the $\hat{\mathbf{x}}$- and $\hat{\mathbf{y}}$-polarized elements.

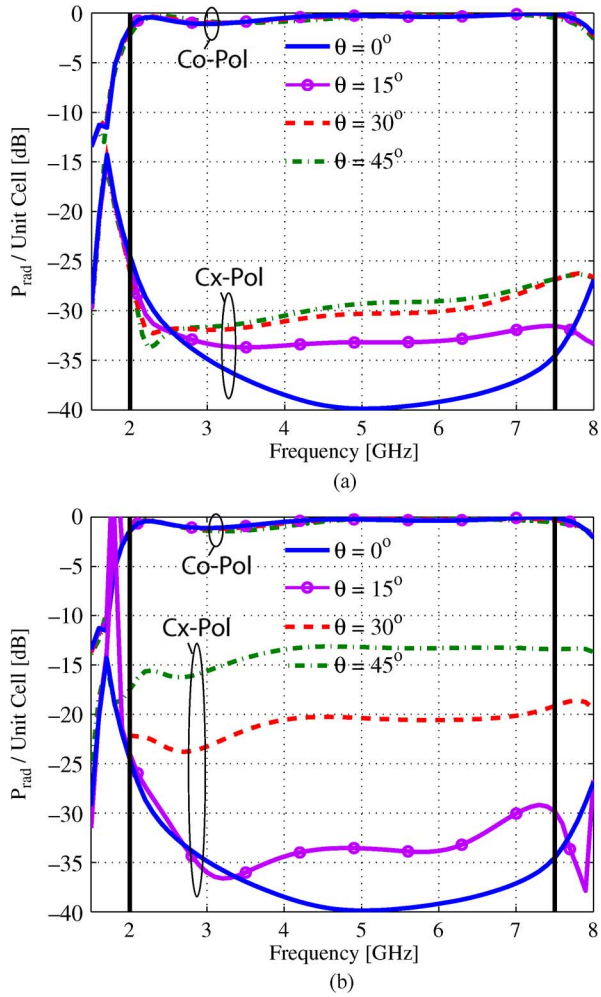

Fig. 19. Co- and cross-polarization radiated power versus frequency and scan angle of the infinite dual-polarized BTA array. (a) E-plane; (b) D-plane. The H-plane polarization levels (not shown here) are approximately the the same as the E-plane.

The E-plane scan has the best cross-polarization performance, with levels between -27 dB and -40 dB. The H-plane (not shown here) had similar cross-polarization behavior with levels below -25 dB. The D-plane exhibits higher cross-polarization levels than the principle planes, as observed in the single-pol BTA of Section V-A2, but this dual-pol array has a notably better performance, reaching a maximum level of -14 dB for $\theta = 45°$. These results are consistent with observations reported in [29], which found single-polarized arrays to have a much higher change in their polarization state when they are scanned away from broadside, as compared to dual-polarized arrays.

VI. CONCLUSION

The BTA array achieves wideband operation over a wide scan volume, while maintaining good polarization purity. The array uses modular, low-profile, vertically integrated PCB elements that are fed directly by standard unbalanced RF interfaces. The conception of the array was based on insights gained from a simple resonant model, which was developed to predict

the common-mode resonance encountered in balanced fin arrays fed by unbalanced feeds. The BTA uses shorting posts that connect each element fin to the ground, effectively tuning the common mode out-of-band. The addition of the shorting posts has other performance implications, which were also described using simple models that provide insight into the low frequency operation and offer design guidelines. Asymmetric placement of the shorting posts was found to result in the best performance and led to single- and dual-polarized infinite BTA arrays with 3.75:1 bandwidths out to $\theta = 45°$. The maximum cross-polarization level at $\theta = 45°$ in the D-plane was -10 dB and -14 dB for the single- and dual-polarized designs, respectively.

REFERENCES

[1] G. C. Tavik, C. L. Hilterbrick, J. B. Evins, J. J. Alter, J. G. Crnkovich, J. W. de Graaf, W. Habicht, G. P. Hrin, S. A. Lessin, D. C. Wu, and S. M. Hagewood, "The advanced multifunction RF concept," *IEEE Trans. Microw. Theory Tech.*, vol. 53, no. 3, pp. 1009–1020, Mar. 2005.

[2] K. Trott, B. Cummings, R. Cavener, M. Deluca, J. Biondi, and T. Sikina, "Wideband phased array radiator," in *Proc. IEEE Int. Symp. Phased Array Systems and Technology*, 2003, pp. 383–386.

[3] P. J. Hall, R. T. Schilizzi, P. E. F. Dewdney, and T. J. W. Lazio, "The square kilometer array (SKA) radio telescope: Progress and technical directions," *URSI Radio Science Bulletin*, no. 326, pp. 4–19, Sep. 2008.

[4] S. Balling, M. Hein, M. Hennhofer, G. Sommerkorn, R. Stephan, and R. Thoma, "Broadband dual polarized antenna arrays for mobile communication applications," in *Proc. 33rd Eur. Microwave Conf.*, Oct. 2003, vol. 3, pp. 927–930.

[5] , R. A. York and Z. B. Popovic, Eds., *Active and Quasi-Optical Arrays for Solid-State Power Combining*, ser. Wiley Series in Microwave and Optical Engineering. New York: Wiley, 1997.

[6] M. V. Ivashina, M. Kehn, P. S. Kildal, and R. Maaskant, "Decoupling efficiency of a wideband Vivaldi focal plane array feeding a reflector antenna," *IEEE Trans. Antennas Propag.*, vol. 57, pp. 373–382, Feb. 2009.

[7] W. Croswell, T. Durham, M. Jones, D. Schaubert, P. Friederich, and J. Maloney, "Wideband antenna arrays," in *Modern Antenna Handbook*, C. A. Balanis, Ed. New York: Wiley, 2008.

[8] T. Chio and D. Schaubert, "Parameter study and design of wide-band widescan dual-polarized tapered slot antenna arrays," *IEEE Trans. Antennas Propag.*, vol. 48, no. 6, pp. 879–886, Jun. 2000.

[9] M. Kragalott, W. R. Pickles, and M. Kluskens, "Design of a 5:1 bandwidth stripline notch array from FDTD analysis," *IEEE Trans. Antennas Propag.*, vol. 48, no. 11, pp. 1733–1741, Nov. 2000.

[10] N. Schuneman, J. Irion, and R. Hodges, "Decade bandwidth tapered notch antenna array element," in *2001 Antenna Applications Symp.*, Allerton Park, Monticello, IL, Sep. 2001.

[11] M. Stasiowski and D. H. Schaubert, "Broadband array antenna," in *2008 Antenna Applications Symp.*, Allerton Park, Monticello, IL, Sep. 2008.

[12] H. Holter, "Dual-polarized broadband array antenna with BOR-elements, mechanical design and measurements," *IEEE Trans. Antennas Propag.*, vol. 55, no. 2, pp. 305–312, Feb. 2007.

[13] E. W. Lucas, M. A. Mongilio, K. M. Leader, C. P. Stieneke, and J. W. Cassen, "Notch radiator elements," U.S. patent 5,175,560, Dec. 29, 1992.

[14] H. Loui, J. P. Weem, and Z. Popovic, "A dual-band dual-polarized nested Vivaldi slot array with multi-level ground planes," *IEEE Trans. Antennas Propag.*, vol. 51, pp. 2168–2175, Sep. 2003.

[15] J. D. S. Langley, P. S. Hall, and P. Newham, "Balanced antipodal Vivaldi antenna for wide bandwidth phased arrays," *IEE Proc.—Microwaves, Antennas and Propagation*, vol. 143, no. 2, pp. 97–102, Apr. 1996.

[16] M. W. Elsallal and D. H. Schaubert, "Reduced-height array of balanced antipodal vivaldi antennas (bava) with greater than octave bandwidth," in *2005 Antenna Applications Symp.*, Allerton Park, Monticello, IL, Sep. 2005, pp. 226–242.

[17] J. J. Lee, S. Livingston, and R. Koenig, "Performance of a wideband (3–14 GHz) dual-pol array," in *Proc. 2004 IEEE Antennas and Propagation Society Int. Symp.*, Jun. 2004, vol. 1, pp. 551–554.

[18] J. J. Lee, S. Livingston, and R. Koenig, "A low-profile wide-band (5:1) dual-pol array," *IEEE Antennas Wireless Propag. Lett.*, vol. 2, pp. 46–49, 2003.

[19] M. Elsallal, "Doubly-Mirrored Balanced Antipodal Vivaldi Antenna (Dm-BAVA) for high performance arrays of electrically short, modular elements," Ph.D. dissertation, Dept. Electr. Comput. Eng., Univ. Massachusetts, Amherst, MA, 2007.

[20] S. G. Hay and J. D. O'Sullivan, "Analysis of common-mode effects in a dual polarized planar connected-array antenna," *Radio Science, RS6S04*, vol. 43, Dec. 2008.

[21] E. de Lera Acedo, E. Garcia, V. Gonzalez-Posadas, J. L. Vazquez-Roy, R. Maaskant, and D. Segovia, "Study and design of a differentially-fed tapered slot antenna array," *IEEE Trans. Antennas Propag.*, vol. 58, no. 1, pp. 68–78, Jan. 2010.

[22] S. Edelberg and A. A. Oliner, "Mutual coupling effects in large antenna arrays II: Compensation effects," *IRE Trans. Antennas Propag.*, vol. 8, no. 4, pp. 360–367, Jul. 1960.

[23] J. R. Bayard, D. H. Schaubert, and M. E. Cooley, "E-plane scan performance of infinite arrays of dipoles printed on protruding dielectric substrates: Coplanar feed line and E-plane metallic wall effects," *IEEE Trans. Antennas Propag.*, vol. 41, no. 6, pp. 837–841, Jun. 1993.

[24] Ansoft HFSS. ver. 11.2. [Online]. Available: www.ansoft.com

[25] D. Cavallo, A. Neto, and G. Gerini, "PCB slot based transformers to avoid common-mode resonances in connected arrays of dipoles," *IEEE Trans. Antennas Propag.*, vol. 58, pp. 2767–2771, Aug. 2010.

[26] S. S. Holland, M. N. Vouvakis, and D. H. Schaubert, "Modular wideband antenna array," U.S. patent application 61/230,768, Aug. 3, 2009.

[27] S. S. Holland, M. N. Vouvakis, and D. H. Schaubert, "A new modular wideband array topology," in *2009 Antenna Applications Symp.*, Allerton Park, Monticello, IL, Sep. 2009.

[28] A. Ludwig, "The definition of cross polarization," *IEEE Trans. Antennas Propag.*, vol. 21, pp. 116–119, Jan. 1973.

[29] D. T. McGrath, N. Schuneman, T. H. Shively, and J. Irion, II, "Polarization properties of scanning arrays," in *Proc. IEEE Int. Symp. Phased Array Systems and Technology*, Oct. 2003, pp. 295–299.

Steven S. Holland (S'05) was born in Chicago, IL, in 1984. He received the B.S. degree in electrical engineering from the Milwaukee School of Engineering (MSOE), Milwaukee, WI, in 2006. Since 2006, he has been with the Antennas and Propagation Laboratory at the University of Massachusetts Amherst, where he received the M.S. degree in 2008 and is currently working towards the Ph.D. degree, both in electrical engineering.

HIs research interests include ultra-wideband phased arrays and electrically small antennas.

Mr. Holland is a member of Tau Beta Pi.

Marinos N. Vouvakis (S'99–M'05) received the Diploma degree in electrical engineering, from Democritus University of Thrace (DUTH), Xanthi, Greece, in 1999. He received the M.S. degree from Arizona State University (ASU), Tempe, AZ, and the Ph.D. degree from The Ohio State University (OSU), Columbus, OH, both in electrical and computer engineering.

Currently he is an Assistant Professor with the Center for Advanced Sensor and Communication Antennas in the Electrical and Computer Engineering Department, University of Massachusetts at Amherst. His research interests are in the area of computational electromagnetics with emphasis on domain decomposition, fast finite element and integral equation methods, hybrid methods, model order reduction and unstructured meshing for electromagnetic radiation and scattering applications. His interests extend to the design and manufacturing of ultra-wideband phased array systems.